An Interface Co-modification Strategy for Improving the Efficiency and Stability of $CsPbI_3$ Perovskite Solar Cells

Guan, Hui; Lei, Yutian; Wu, Qiyuan; Zhou, Xufeng; Wang, Haoxu; Wang, Gang; Li, Wenquan; Jin, Zhiwen; Lan, Wei

DOI
10.1021/acsaem.2c02096

Publication date
2022

Document Version
Final published version

Published in
ACS Applied Energy Materials

ACS APPLIED ENERGY MATERIALS

www.acsaem.org Article

An Interface Co-modification Strategy for Improving the Efficiency and Stability of $CsPbI_3$ Perovskite Solar Cells

Hui Guan, Yutian Lei, Qiyuan Wu, Xufeng Zhou, Haoxu Wang, Gang Wang, Wenquan Li, Zhiwen Jin,* and Wei Lan*

Cite This: *ACS Appl. Energy Mater.* 2022, 5, 13419−13428 Read Online

ACCESS | Metrics & More | Article Recommendations | Supporting Information

ABSTRACT: Interface engineering is a simple and effective strategy for improving the photovoltaic performance and stability of perovskite solar cells (PSCs). Herein, an interface co-modification strategy is proposed, using [6,6]-phenyl-C61-butyric acid methyl ester (PCBM) and 2-fluoro-1,4-phenylenediammonium iodide (2FPPD) to modify the electron transport layer (ETL)/perovskite (PVK) and the PVK/hole transport layer (HTL) interfaces, respectively. A series of characterizations demonstrate that the PCBM&2FPPD interface co-modification strategy effectively enhances the extraction and transport efficiency of carriers at the interface, passivates surface defects, inhibits the nonradiative recombination of carriers, and simultaneously inhibits ion migration. Moreover, this strategy improves the crystallinity and surface hydrophobicity of PVK and optimizes the energy level alignment of PSCs. As a result, all photovoltaic parameters are improved after optimization, where the power conversion efficiency (PCE) of PSCs has increased from 17.01% to 18.36%. Meanwhile, the optimized PSCs show excellent environmental stability, which can be stably stored in air (RH = 10−20%) for about 800 h.

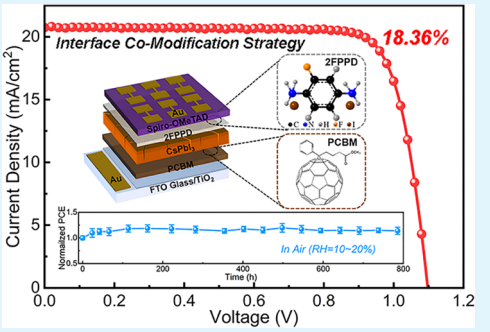

KEYWORDS: *perovskite solar cell, $CsPbI_3$, interface engineering, defect passivation, photovoltaic performance, stability*

1. INTRODUCTION

Halide perovskites are considered to be one of the most popular candidate materials for third-generation solar cells due to low defect density, high carrier mobility, long exciton lifetime and diffusion length, and low cost.[1,2] Since the first report in 2009, the power conversion efficiency (PCE) of laboratory-scale perovskite solar cells (PSCs) has significantly increased from 3.8% to 25.7%.[3,4] Interestingly, the all-inorganic perovskites, which have no volatile components, exhibit better chemical stability than the organic−inorganic hybrid perovskites (OIHPs) that are currently being studied.[5−7] Among them, $CsPbI_3$ perovskite has a universal bandgap of ∼1.7 eV, which is a kind of excellent light-absorbing material for single-junction solar cells and top light-absorbing material for tandem solar cells.[8,9]

Unfortunately, the photovoltaic performance of $CsPbI_3$ PSCs is inferior to that of OIHP solar cells due to limitations such as high defect density, low charge extraction and transport efficiency, and ion migration.[10,11] In particular, the perovskite phase $CsPbI_3$ (black phase) is easily converted to non-perovskite phase $CsPbI_3$ (yellow phase) by low effective coordination of Cs^+ and $[PbI_6]^{4-}$ octahedra and destruction of water and oxygen.[12,13] Meanwhile, it has been confirmed that there are unavoidable defects in $CsPbI_3$ films, such as Cs^+ vacancies, Pb^{2+} coordination defects, etc., which will cause serious carrier non-radiative recombination.[14] For the above problems, extensive research has shown that interface engineering is one of the most simple and effective strategies.[1,11,15−17] In 2019, Liu et al. developed nitrogen-doped graphene quantum dots (N-GQDs) and deposited them on top of $CsPbI_3$, which increased the PCE from 15.53% to 16.02%.[18] In 2020, Jin et al. used guanidine hydrobromide (GABr) to treat the surface of $CsPbI_3$, and the PCE of optimized PSCs reached 18.02%.[19] Recently, Zhao et al. achieved crystal secondary growth through the solid-state reaction between *N,N,N*-trimethyl-1-dodecanaminium bromide (DTABr) and $CsPbI_3$, resulting in a PCE of 20.04% and excellent operational stability.[20]

Generally, planar heterojunction PSCs are a sandwich structure of an electron transport layer (ETL)/perovskite (PVK)/hole transport layer (HTL). The contact and matching between interfaces are some of the non-negligible factors affecting the photovoltaic performance and stability of PSCs.[21,22] On the one hand, interface engineering can modify the ETL/PVK interface (buried interface of PVK).[23−26]

Received: July 4, 2022
Accepted: October 14, 2022
Published: October 27, 2022

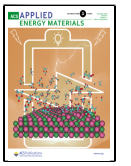

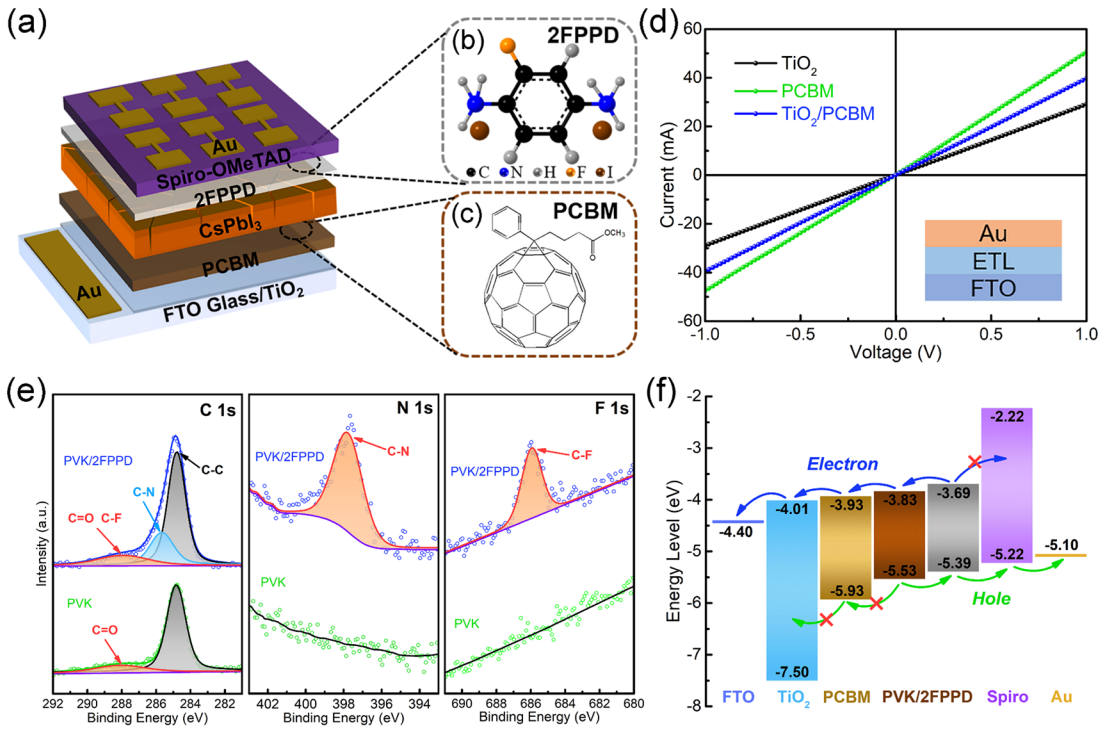

Figure 1. (a) Schematic of the device structure; (b, c) molecular structures of 2FPPD and PCBM; (d) *I*−*V* characteristics of FTO/TiO_2/Au, FTO/PCBM/Au, and FTO/TiO_2/PCBM/Au, where the inset is the device structure; (e) C 1s, N 1s, and F 1s XPS core-level spectra of PVK and PVK/2FPPD; (f) schematic energy level diagram of PSCs based on PCBM/PVK/2FPPD.

Currently, the commonly used ETL material TiO_2 has disadvantages such as lower conductivity and higher defect density, which limit the extraction and transport efficiency of carriers at the ETL/PVK interface.[27−29] Bao et al. modified TiO_2 with n-type doped [6,6]-phenyl-C61-butyric acid methyl ester (N-doped PCBM), which significantly improved the extraction and transport efficiency of carriers and reduced the energy shift.[30] On the other hand, suitable organic molecules (containing $-NH_2$, −OH, etc.) can be used to modify the PVK/HTL interface (upper interface of PVK).[31−33] These molecules can interact with those uncoordinated Pb^{2+} defects on the surface of PVK through Lewis acid−base interactions, which can passivate the defects at the interface and optimize the quality of PVK films.[34] Moreover, organic molecules can act as moisture barriers due to their strong hydrophobicity to prevent PVK from being damp and undergoing phase transition.[35] For example, Yang et al. formed a 2D/3D hybrid structure at the PVK/HTL interface by introducing 4-trifluoromethylphenetylammonium iodide (CF_3PEAI), where the 2D structure played an important role in optimizing energy band alignment, passivating defects, and protecting 3D structure.[36] Furthermore, the dual passivation strategy has also been widely used to optimize the performance and stability of PSCs.[37−41] For example, Zhu et al. reported a deep-dependent manipulation strategy through a binary modulation system to passivate PVK grain boundaries and surfaces, which achieved the overall defect management.[42]

In this work, we adopted an interface co-modification strategy, using [6,6]-phenyl-C61-butyric acid methyl ester (PCBM) and 2-fluoro-1,4-phenylenediammonium iodide (2FPPD) to simultaneously modify the buried interface and upper interface of $CsPbI_3$, which improved the photovoltaic performance and stability of PSCs. Compared with the pristine (control), the PCBM single-layer interface modification (PCBM/PVK), and the 2FPPD single-layer interface modification (PVK/2FPPD) PSCs, the PSCs of the PCBM&2FPPD interface co-modification strategy (PCBM/PVK/2FPPD) showed lower defect density, less carrier interface recombination and ion migration, and higher carrier mobility. Particularly, the PCBM thin layer improved the conductivity of ETL, which enhanced the extraction and transport efficiency of carriers at the ETL/PVK interface. The 2FPPD thin layer passivated those uncoordinated Pb^{2+} defects and promoted the crystal secondary growth through Lewis acid−base interactions, which improved the crystallinity of $CsPbI_3$. Meanwhile, the 2FPPD thin layer played an important role in blocking moisture due to its strong hydrophobicity. Furthermore, this strategy optimized the energy level alignment of PSCs, which reduced the energy barrier of carrier transport. Finally, the PSCs with a PCE of 18.36% were obtained and showed much enhanced stability.

2. RESULTS AND DISCUSSION

As shown in Figure 1a, the structure of PSCs based on the PCBM&2FPPD interface co-modification strategy is FTO/TiO_2/PCBM/$CsPbI_3$/2FPPD/2,2′,7,7′-tetrakis[*N*,*N*-di-*p*-methoxyphenylamine]-9,9′-spirobifluorene (Spiro-OMeTAD)/Au, in which 2FPPD (Figure 1b) and PCBM (Figure 1c) are used to modify the bilateral interfaces of $CsPbI_3$. The schematic diagram of the preparation process for the PCBM&2FPPD interface co-modification strategy is shown in Figure S1. It is worth mentioning that the surface of the PCBM thin layer has poor wettability. Therefore, the methods to improve the wettability of the PCBM thin layer were explored (Figures S2−S4). The affinity between perovskite precursor solution and ETL is one of the important factors affecting the quality of perovskite films.[30] As shown in Figure S4, the perovskite precursor solution contact angle of TiO_2/

https://doi.org/10.1021/acsaem.2c02096
ACS Appl. Energy Mater. 2022, 5, 13419−13428

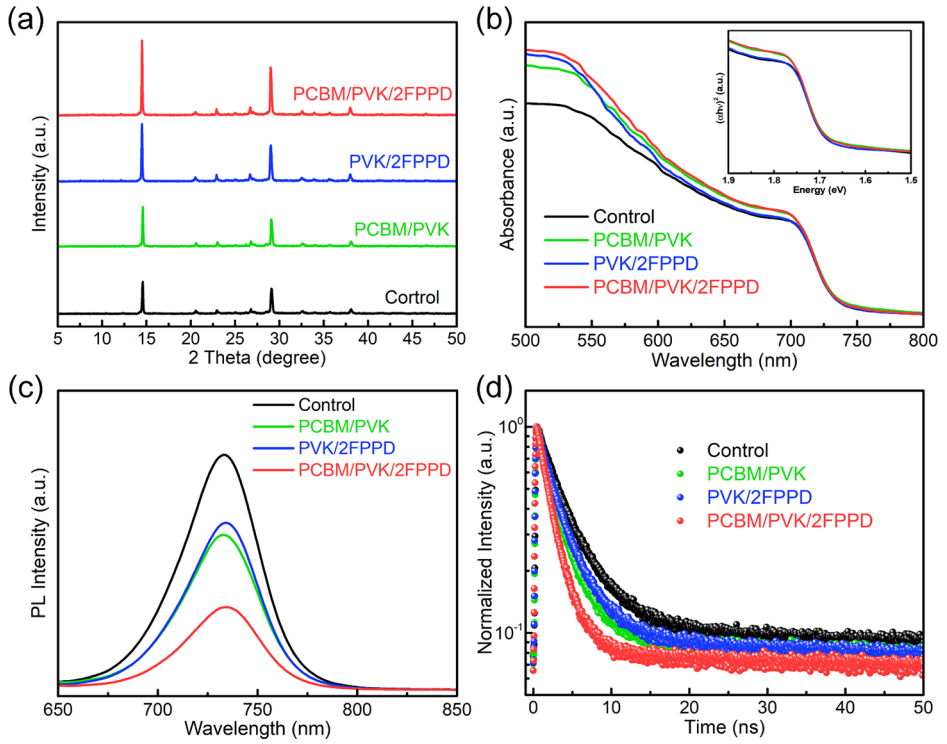

Figure 2. (a) XRD patterns, (b) UV−vis absorption spectra, (c) steady-state PL spectra, and (d) TRPL spectra of control, PCBM/PVK, PVK/2FPPD, and PCBM/PVK/2FPPD films, respectively.

PCBM is 34.4°, which is not conducive to the formation of high-quality perovskite films. However, after modification of the PCBM thin layer surface with DMF, the perovskite precursor solution contact angle changes to 8.3°, indicating that the affinity between the precursor solution and PCBM thin layer is greatly increased, which will be beneficial to the formation of high-quality thin films.

Figure S5 and Figure 1d demonstrate the positive effects on PSCs with the PCBM thin layer inserted. The optical transmission spectra in Figure S5 show that the average transmittance values at 550−700 nm of FTO, FTO/TiO_2, and FTO/TiO_2/PCBM films are 81.57%, 82.22%, and 82.08%, respectively. Obviously, the PCBM thin layer does not significantly reduce the transmittance of ETL, which provides convenient conditions for preparation of PSCs. Moreover, the current−voltage (I−V) characterization curves of different ETLs were measured (Figure 1d), and the film conductivity (σ) was calculated according to following formula:[43]

$$\sigma = \frac{Id}{VA} \tag{1}$$

where d is the thickness of films and A is the area of devices. Table S1 shows the calculated parameters and results. The conductivity of the TiO_2/PCBM film is 2.64×10^{-3} mS cm^{-1}, which is higher than those of the pure TiO_2 film (1.60×10^{-3} mS cm^{-1}) and PCBM film (2.18×10^{-3} mS cm^{-1}). The enhancement of ETL conductivity improves the carrier transport efficiency at the ETL/PVK interface, which facilitates the increase in J_{SC}.[44]

Alternatively, X-ray photoelectron spectroscopy (XPS) was used to explore the existence of 2FPPD and its interaction mechanism with PVK (Figure 1e and Figure S6). Figure 1e demonstrates the existence of 2FPPD, where the increased peak areas of PVK/2FPPD at 284.8 and 287.8 eV in the C 1s XPS core-level spectra are attributed to the C−C bond and C−F bond of 2FPPD; the peaks at 398.4 eV in the N 1s XPS core-level spectra and 285.6 eV in the C 1s XPS core-level spectra are attributed to the C−N bond of 2FPPD; the peak at 685.7 eV in the F 1s XPS core-level spectra is attributed to the C−F bond of 2FPPD.[36,45] Moreover, the XPS core-level spectra of the main elements (Cs, Pb, I) in PVK were measured to explore the interaction mechanism (Figure S6b−d). As shown in Figure S6c, two main peaks (Pb 4f5/2 and Pb 4f7/2) corresponding to the Pb element of PVK/2FPPD shift by 0.13 eV to a higher binding energy, indicating that the coordination environment of the Pb element has changed.[46] It is attributed to the Lewis interaction of 2FPPD with uncoordinated Pb^{2+}, which passivates the defects on the PVK surface.

Furthermore, the energy level alignment of PSCs must have been changed after PCBM&2FPPD co-modification, so valence band X-ray photoelectron spectroscopy (VB XPS) and ultraviolet photoelectron spectroscopy (UPS) were deployed for characterization (Figure S7), which can reveal the energy level shift of the film surface.[47] The VB XPS spectra (Figure S7a) show that the VB energy of PVK/2FPPD is reduced, indicating that the semiconductor type of PVK/2FPPD shifts to p-type and there exists deeper band bending, which can help to reduce the energy barrier between PVK and HTL.[48,49] Meanwhile, UPS was used to characterize the energy level alignment of PSCs (Figure S7b−d). The work function (WF) can be calculated by the cut-off energy (E_{cutoff}) region (Figure S7c) according to following formula: $WF = 21.22 - E_{cutoff}$ (eV), where 21.22 eV is the energy of ultraviolet photoelectrons. The calculated WFs of PCBM, PCBM/PVK, and PCBM/PVK/2FPPD are 4.26, 4.05, and 4.04 eV, respectively. Apparently, the VB energy can be calculated by the Fermi energy (E_{Fermi}) region (Figure S7d), so that the VB energies of PCBM, PCBM/PVK, and PCBM/PVK/2FPPD are

https://doi.org/10.1021/acsaem.2c02096
ACS Appl. Energy Mater. 2022, 5, 13419−13428

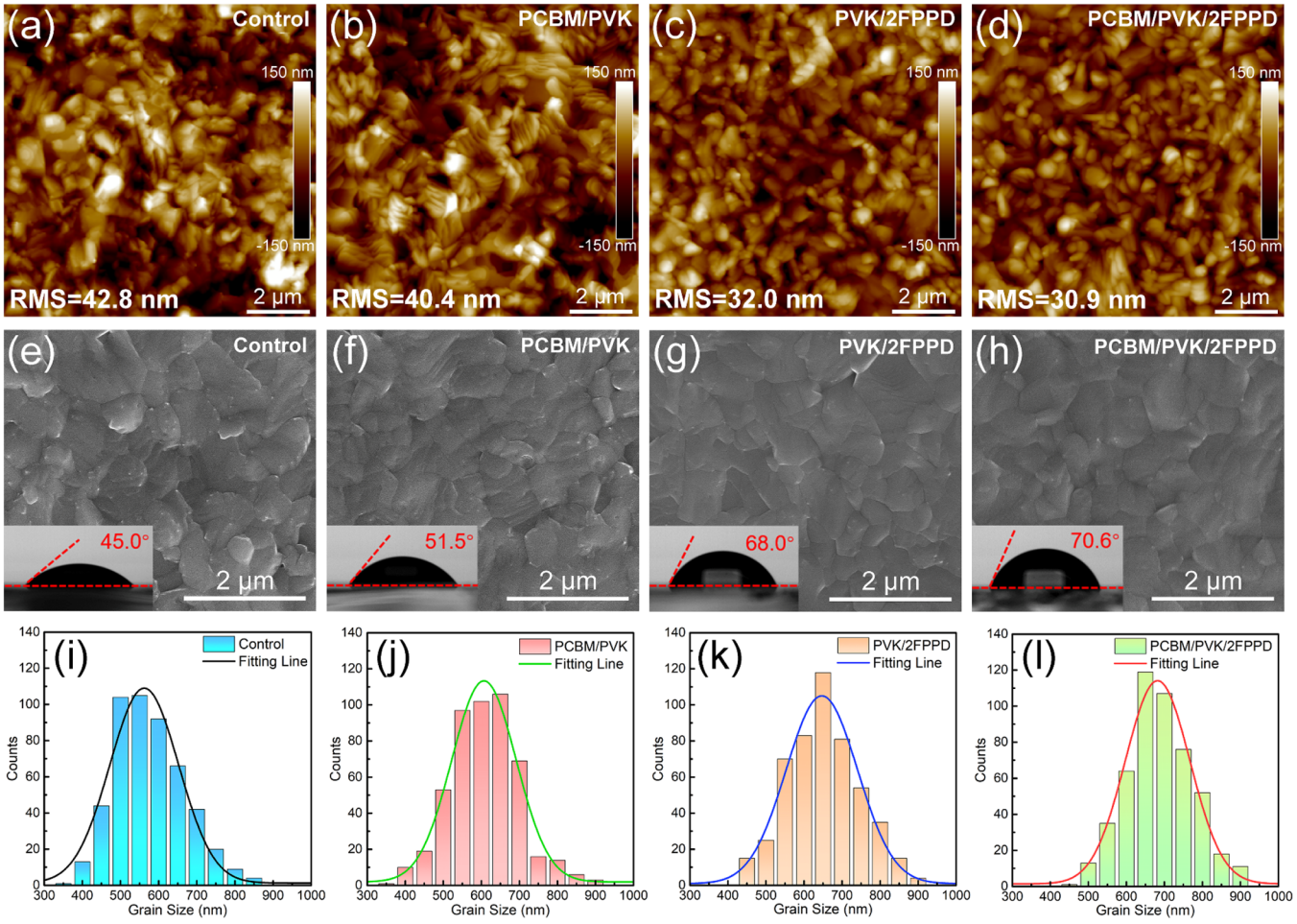

Figure 3. (a–d) AFM images, (e–h) top-view morphological SEM images, where the insets show the water contact angle, and (i–l) grain size distribution of control, PCBM/PVK, PVK/2FPPD, and PCBM/PVK/2FPPD films, respectively.

1.67, 1.48, and 1.35 eV, respectively. Therefore, the VB maximum energy of PCBM, PCBM/PVK, and PCBM/PVK/2FPPD can be obtained, which are −5.93, −5.53, and −5.39 eV, respectively. Finally, according to the energy gap of PCBM (∼2.0 eV), PCBM/PVK (∼1.7 eV), and PCBM/PVK/2FPPD (∼1.7 eV) (Figure 2b,c), the conduction band (CB) minimum energy of PCBM, PCBM/PVK, and PCBM/PVK/2FPPD can be calculated, which are −3.93, −3.83, and −3.69 eV, respectively. Therefore, the schematic diagram of the PSC energy level alignment based on PCBM/PVK/2FPPD was obtained as shown in Figure 1f.[30,47,50] The PCBM&2FPPD interface co-modification strategy reduces the energy level shift, provides stairs for interfacial carrier transport, and inhibits interfacial recombination simultaneously.

To reveal the influence of the PCBM&2FPPD interface co-modification strategy on PVK crystallization, XRD patterns of control, PCBM/PVK, PVK/2FPPD, and PCBM/PVK/2FPPD were measured (Figure 2a and Figure S8). It is worth mentioning that the diffraction peaks of 14.38° and 28.85° corresponding to the (110) and (220) crystal planes are not shifted, indicating that the insertion of PCBM and 2FPPD thin layers does not cause in-lattice stress or size change of the lattice in PVK. Meanwhile, the full width at half-maximum (FWHM) of the diffraction peak corresponding to the (110) crystal plane is reduced (Table S2), from 0.140 (control) to 0.121 (PCBM/PVK), 0.118 (PVK/2FPPD), and 0.112 (PCBM/PVK/2FPPD), indicating that the crystal orientation toward the (110) crystal plane increases the PVK crystallinity.[32,51] Particularly, the increase of diffraction peak intensity is observed with insertion of the 2FPPD thin layer. The 2FPPD promotes crystal secondary growth leading to improvement in the crystallinity of PVK.[20]

The ultraviolet–visible (UV–vis) absorption spectra in Figure 2b and Figure S9 show that the influence of PCBM and 2FPPD thin layers on the PVK optical band gap is negligible while the absorption intensity has been strengthened, which contributes to the improvement of J_{SC}. Moreover, the steady-state photoluminescence (PL) spectra show that the PL intensity is significantly reduced with PCBM and 2FPPD thin layers inserted (Figure 2c and Figure S10). There are two possibilities for this phenomenon: (1) The PCBM thin layer enhances the extraction and transport efficiency of carriers at interface. (2) The 2FPPD thin layer passivates the defects on the PVK surface and reduces non-radiative recombination. Figure 2d shows the time-resolved PL (TRPL) spectra, and the parameters obtained by bi-exponential decay function fitting are shown in Table S3. Generally, slow decay (τ_1) is considered to be related to the defect density in PVK. Since defects are one of the causes of carrier non-radiative recombination, the longer the τ_1, the lower the defect density in PVK. Fast decay (τ_2) is believed to be related to the extraction and transport of carriers at the interface, so the shorter the τ_2 is, the higher the extraction and transport efficiency of carriers at the interface gained.[44,52] In comparison,

https://doi.org/10.1021/acsaem.2c02096
ACS Appl. Energy Mater. 2022, 5, 13419−13428

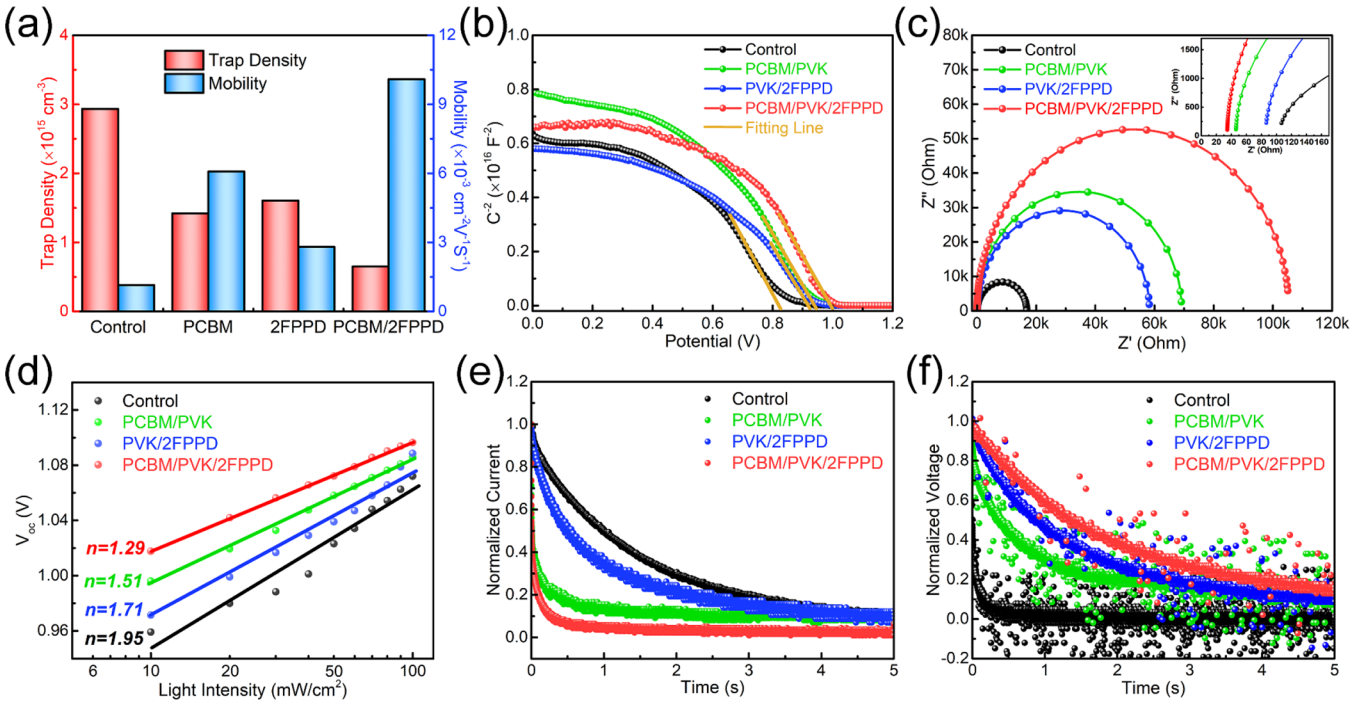

Figure 4. (a) Trap density and mobility statistical histogram calculated by dark $J-V$ curves for electron-only devices; (b) Mott−Schottky plots, (c) Nyquist plots, (d) V_{OC} as a function of light intensity, (e) TPC, and (f) TPV based on control, PCBM/PVK, PVK/2FPPD, and PCBM/PVK/2FPPD PSCs, respectively.

τ_1 increases from 29.86 ns (control) to 34.39 ns (PCBM/PVK), 33.39 ns (PVK/2FPPD), and 41.64 ns (PCBM/PVK/2FPPD), indicating that defect density is reduced and the quality of PVK is improved. Meanwhile, τ_2 is reduced from 3.45 ns (control) to 2.44 ns (PCBM/PVK), 2.84 ns (PVK/2FPPD), and 1.82 ns (PCBM/PVK/2FPPD), indicating that the extraction and transport efficiency of carriers at the ETL/PVK interface is improved. The above results of TRPL spectra are consistent with the steady-state PL spectra.

Figure 3a−d shows the atomic force microscope (AFM) height mode images of PVK (3D AFM images shown in Figure S11). The insertion of PCBM and 2FPPD thin layers reduces the root mean square (RMS) roughness of the PVK surface, from 42.8 nm (control) to 40.4 nm (PCBM/PVK), 32.0 nm (PVK/2FPPD), and 30.9 nm (PCBM/PVK/2FPPD). In particular, the RMS is significantly reduced due to the insertion of the 2FPPD thin layer, leading us to speculate that 2FPPD is intended to be located at grain boundaries on the surface of PVK, which reduces the height difference of the PVK surface. In order to further verify the state of 2FPPD on the surface of PVK, the phase imaging mode of AFM was applied (Figure S12). By comparison, it is found that 2FPPD presents a regional distribution on the surface of PVK and is distributed more at the grain boundaries, which does not completely cover the PVK surface. It is worth mentioning that Kyaw et al. also formed a localized 2D/3D heterostructure on the surface of PVK.[53] Compared with full coverage, regional coverage of 2FPPD on the PVK surface does not hinder the transport of carriers between PVK and HTL but passivates uncoordinated Pb^{2+} defects on the PVK surface and improves the humidity stability of PVK.

The morphology of PVK was demonstrated from scanning electron microscope (SEM) images (Figure 3e−h and Figures S13 and S14). The statistical distribution of grain size shows that the average grain size becomes larger with PCBM and 2FPPD thin layers inserted (Figure 3i−l). Clearly, the average grain sizes of PCBM/PVK, PVK/2FPPD, and PCBM/PVK/2FPPD are 608, 649, and 682 nm, respectively, while the average grain size of the control is 562 nm. In particular, the insertion of PCBM & 2FPPD bilayers increases the grain size by 120 nm. There are two main reasons for the above phenomenon: (1) the thin layer of DMF-treated PCBM improves the quality of PVK formation; (2) 2FPPD as a Lewis base reacts with uncoordinated Pb^{2+} as a Lewis acid to passivate the defects, and this solid-state reaction promotes the secondary growth of the grain size.[20,30,34] The larger grain size means that there are fewer grain boundaries and fewer defects in PVK, which helps to improve the performance of PSCs. Analogously, the SEM images show that the surface of PVK is flatter with a 2FPPD thin layer inserted, which is consistent with the results of AFM. Meanwhile, the water contact angle of PVK was also characterized (the insets of Figure 3e−h). It is found that the water contact angle increased from 45.0° (control) to 51.5° (PCBM/PVK), 68.0° (PVK/2FPPD), and 70.6° (PCBM/PVK/2FPPD). The increase in contact angle after PCBM thin layer insertion is attributed to the improved film formation quality of PVK by DMF treatment, indicating that fewer defects are formed in PVK. Especially, the water contact angle increases significantly (from 45.0° to 68.0°) with 2FPPD thin layer inserted, which is due to the strong hydrophobicity of 2FPPD. Correspondingly, the hydrophobicity of 2FPPD can significantly improve the humidity stability of PVK and further provide PSCs with outstanding environment stability.

Subsequently, in order to further investigate trap density and carrier mobility, the space-charge-limited current (SCLC) was measured. On the one hand, the electron-only devices were prepared for the control, PCBM/PVK, PVK/2FPPD, and

https://doi.org/10.1021/acsaem.2c02096
ACS Appl. Energy Mater. 2022, 5, 13419−13428

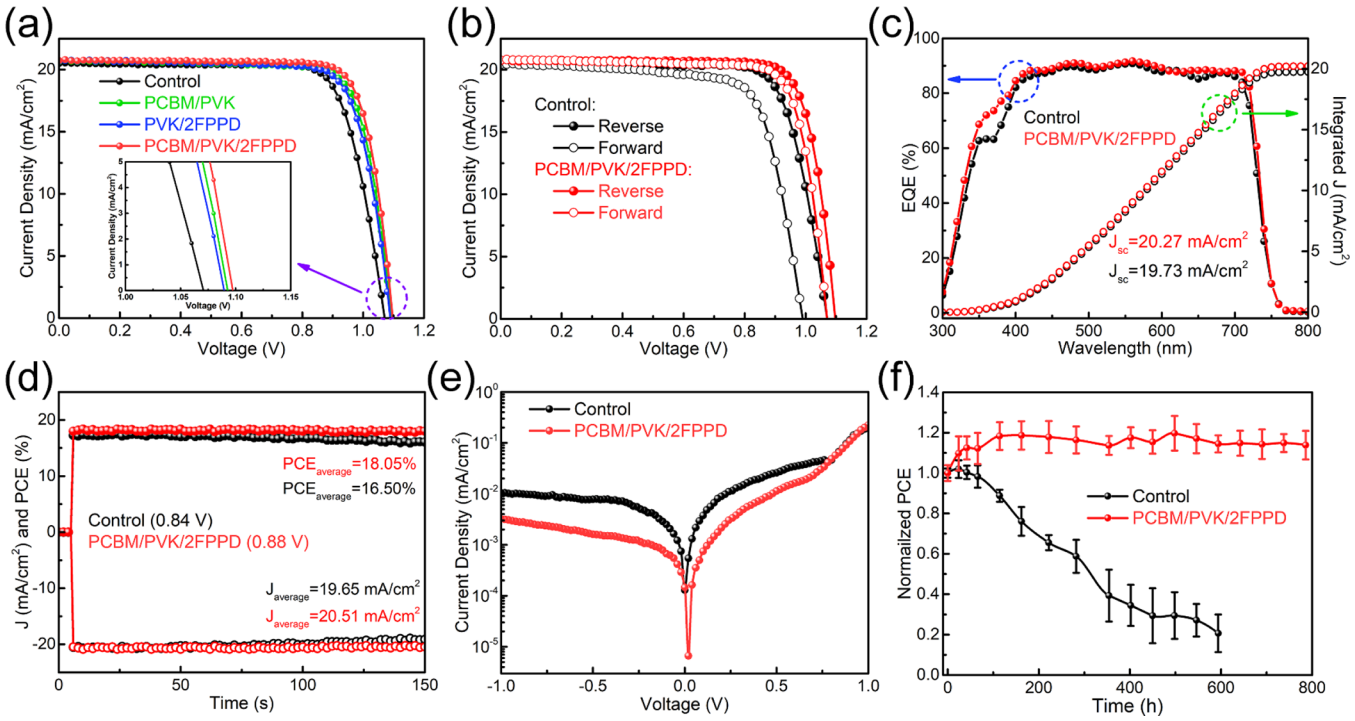

Figure 5. (a) $J-V$ curves; (b) $J-V$ curves of hysteresis behavior, (c) EQE spectra and integrated J curves, (d) steady-state measurement of the photocurrent and PCE, (e) dark $J-V$ curves, and (f) PCE stability stored in air (RH = 10−20%) based on control and PCBM/PVK/2FPPD PSCs.

PCBM/PVK/2FPPD. The corresponding structure and SCLC curves are shown in Figure S15. On the other hand, the hole-only devices were prepared for the control and PVK/2FPPD. The corresponding structure and SCLC curves are shown in Figure S16. Therefore, the trap density (N_{traps}) and carrier mobility (μ) can be calculated by the following formulas:[54]

$$N_{traps} = \frac{2\varepsilon_0\varepsilon_r V_{TFL}}{eL^2} \quad (2)$$

$$J_D = \frac{9}{8}\varepsilon_0\varepsilon_r\mu\frac{V^2}{L^3} \quad (3)$$

where ε_0 is the vacuum permittivity, ε_r is the relative permittivity of PVK, e is the electronic charge, V_{TFL} is the onset voltage of trap-filled limit region (the intersection of trap-filled limit region and ohmic region), L is the thickness of film, which can be obtained from the cross-sectional SEM image (Figure S17), J_D is the dark current density, and V is the applied voltage. The relevant calculated parameters and results are shown in Figure 4a and Table S4. The insertion of PCBM and 2FPPD thin layers significantly reduces the electron trap density, from 2.94×10^{15} cm^{-3} (control) to 1.42×10^{15} cm^{-3} (PCBM/PVK), 1.61×10^{15} cm^{-3} (PVK/2FPPD), and 0.65×10^{15} cm^{-3} (PCBM/PVK/2FPPD). Correspondingly, the insertion of 2FPPD thin layer reduces the hole trap density from 1.82×10^{15} cm^{-3} (control) to 1.10×10^{15} cm^{-3} (PVK/2FPPD). In addition, the carrier mobility also increases significantly, in which the electron mobility increases from 1.14×10^{-3} cm^2 V^{-1} s^{-1} (control) to 6.08×10^{-3} cm^2 V^{-1} s^{-1} (PCBM/PVK), 2.80×10^{-3} cm^2 V^{-1} s^{-1} (PVK/2FPPD), and 10.09×10^{-3} cm^2 V^{-1} s^{-1} (PCBM/PVK/2FPPD). The hole mobility increases from 2.43×10^{-4} cm^2 V^{-1} s^{-1} (control) to 3.17×10^{-4} cm^2 V^{-1} s^{-1} (PVK/2FPPD). Obviously, the PCBM&2FPPD interface co-modification strategy can effectively reduce trap density and increase carrier mobility, which facilitates the reduction of nonradiative recombination and the improvement of carrier transport efficiency between interfaces.

Figure 4b and Figure S18 show the Mott−Schottky plots, which can obtain the built-in potential (V_{bi}) according to the Mott−Schottky formula:[55]

$$\frac{1}{C^2} = \frac{2(V_{bi} - V)}{A^2 e\varepsilon_0\varepsilon_r N_A} \quad (4)$$

where A is the device area and N_A is the carrier concentration. Moreover, the width of the depletion layer (W_p) can be calculated by the formula of $W_p = (2\varepsilon_0\varepsilon_r V_{bi}/eN)^{1/2}$, where N is the trap density.[51] The built-in potential of the device is increased from 0.82 V (control) to 0.94 V (PCBM/PVK), 0.92 V (PVK/2FPPD), and 0.99 V (PCBM/PVK/2FPPD). The increase of V_{bi} and W_p can improve the extraction ability of carriers at the interface and suppress the non-radiative recombination of carriers. Furthermore, the Nyquist plots in Figure 4c and Figure S19 show that series resistance (R_s) decreases and recombination resistance (R_{rec}) increases due to the insertion of PCBM and 2FPPD thin layers, indicating that the extraction and transport efficiency of carriers are enhanced and recombination is inhibited.

In order to further evaluate the influence of carrier recombination behavior on the performance of PSCs, we measured the function of V_{OC} on light intensity (I) according to following formula and obtained the ideality factor (n) through fitting:[56]

$$V_{OC} = \frac{nk_BT}{e}\ln(I) + \text{constant} \quad (5)$$

where k_B is Boltzmann's constant and T is the absolute temperature. Generally, it is believed that the closer to 2 the value of n is, the more dominant the trap-assisted Shockley−Read−Hall (SRH) recombination is. However, the closer to 1

https://doi.org/10.1021/acsaem.2c02096
ACS Appl. Energy Mater. 2022, 5, 13419−13428

the value of n is, the fewer carriers recombine at the interface, which means the more favorable it is to prepare high-performance PSCs.[38,57] As shown in Figure 4d, the insertion of PCBM and 2FPPD thin layers significantly reduces the value of n, from 1.95 (control) to 1.51 (PCBM/PVK), 1.71 (PVK/2FPPD), and 1.29 (PCBM/PVK/2FPPD), respectively, indicating that the SRH recombination is significantly suppressed, which contributes to improving V_{OC} and FF of PSCs. Additionally, J_{SC} shows good linearity as a function of light intensity ($J_{SC} \propto I$), indicating that the bimolecular radiative in PSCs is negligible (Figure S20).[42,58]

Furthermore, the transient photocurrent (TPC) and transient photovoltage (TPV) were measured to further explore the carrier dynamics of PSCs.[34,52] TPC shows that the carrier transport lifetime is reduced from 1846 ms (control) to 345 ms (PCBM/PVK), 902 ms (PVK/2FPPD), and 166 ms (PCBM/PVK/2FPPD) (Figure 4e and Figure S21), which means that the extraction and transport efficiency of carriers have been significantly improved. Particularly, the insertion of the PCBM thin layer increases the conductivity of ETL, which leads to greatly improved carrier extraction and transport efficiency (the carrier transport lifetime reduced from 1846 to 345 ms). Similarly, TPV shows that the carrier recombination lifetime is increased from 127 (control) to 825 ms (PCBM/PVK), 1276 ms (PVK/2FPPD), and 1782 ms (PCBM/PVK/2FPPD) (Figure 4f and Figure S22). It demonstrates that the carrier nonradiative recombination is significantly suppressed and the defect density is reduced, especially the 2FPPD thin layer leading to significant reduction of the carrier recombination lifetime (from 127 to 1276 ms). According to the above results, the PCBM&2FPPD interface co-modification strategy not only improves the extraction and transport efficiency of carriers at the interface but also passivates the defects on the surface of PVK, which is consistent with the conclusions obtained from the steady-state PL spectra and the TRPL spectra.

Therefore, planar heterojunction PSCs were prepared based on the PCBM&2FPPD interface co-modification strategy. Figure 5a and Table S5 show the current density−voltage (J−V) curves measured under AM 1.5G illumination (100 mW/cm^2) and photovoltaic performance parameters of PSCs. For PCBM/PVK/2FPPD PSCs, the photovoltaic performance parameters in reverse scan mode are 1.098 V (V_{OC}), 20.72 mA/cm^2 (J_{SC}), 80.69% (FF), and 18.36% (PCE), while the photovoltaic performance parameters of control PSCs are 1.070 V (V_{OC}), 20.49 mA/cm^2 (J_{SC}), 77.52% (FF), and 17.01% (PCE). For comparison, the photovoltaic performances of PCBM/PVK and PVK/2FPPD PSCs are 1.092 V (V_{OC}), 20.66 mA/cm^2 (J_{SC}), 78.71% (FF), and 17.77% (PCE) and 1.089 V (V_{OC}), 20.68 mA/cm^2 (J_{SC}), 77.84% (FF), and 17.54% (PCE), respectively. Moreover, the influence of PCBM and 2FPPD solution concentration on the photovoltaic performance of PSCs was also explored. When the concentrations of PCBM and 2FPPD solutions are 10 and 1 mg/mL, respectively, PSCs show better performance (Figure S23 and Tables S6 and S7), which is consistent with the results of relevant film characterization (Figures S8−S10). The statistical distribution of photovoltaic performance parameters of PSCs shows excellent repeatability (Figure S24).

Based on the above results, we compared the PCBM/PVK/2FPPD PSCs with the control PSCs carefully. In contrast, the PCE exhibits a notable improvement, from 17.01% to 18.36%. Furthermore, the hysteresis behavior of PSCs was also measured (Figure 5b and Figure S25). The hysteresis index (HI) can evaluate the hysteresis behavior and is calculated according to the following formula:[59]

$$\mathrm{HI} = \frac{\mathrm{PCE}_{\mathrm{Reverse}} - \mathrm{PCE}_{\mathrm{Forward}}}{\mathrm{PCE}_{\mathrm{Reverse}}} \quad (6)$$

where the relevant parameters and results are shown in Table S5. The HI is reduced from 0.13 of the control PSCs to 0.04 of the PCBM/PVK/2FPPD PSCs, among which the PSCs of PCBM/PVK and PVK/2FPPD are 0.08 and 0.09, respectively. The reduction of HI confirms that the PCBM&2FPPD interface co-modification strategy can reduce carrier accumulation and inhibit ion migration at the interface.[60,61] The external quantum efficiency (EQE) spectra of PCBM/PVK/2FPPD PSCs and control PSCs in Figure 5c show a small increase in photoelectric conversion efficiency, and the integrated J_{SC} has increased from 19.73 to 20.27 mA/cm^2, which are consistent with the J−V curves.

The steady-state measurement of photocurrent and PCE shows that the photocurrent and PCE of PCBM/PVK/2FPPD PSCs remained at a relatively stable level after 150 s of continuous light soaking while the control PSCs only maintained 94% (Figure 5d). Approximatively, the dark J−V curves shown in Figure 5e indicate that PCBM/PVK/2FPPD PSCs have a smaller dark current compared to the control PSCs. It is also proven that the PCBM&2FPPD interface co-modification strategy can effectively reduce the defects of PVK, resulting in a smaller leakage current. Moreover, the environmental stability of PSCs was measured. As shown in Figure 5f, the PSCs were stored in air (RH = 10−20%), and the PCE was measured as a function of storage time. The PCBM/PVK/2FPPD PSCs are stored about 800 h, and the PCE remains stable. On the contrary, the control PSCs are stored for about 600 h, and the PCE only maintains 21% of the initial PCE. The improvement in environmental stability is due to the PCBM&2FPPD interface co-modification strategy that inhibits ion migration at the interface and increases the hydrophobicity of the PVK surface (water contact angle increased from 45.0° to 70.6°, the insets of Figure 3e−h).

3. CONCLUSIONS

In summary, the PCBM&2FPPD interface co-modification strategy was used to optimize the photovoltaic performance and environmental stability of PSCs. The PCBM thin layer increases the conductivity of ETL, which enhances the extraction and transport efficiency of carriers at the ETL/PVK interface. The 2FPPD thin layer passivates defects and promotes crystal secondary growth through the interaction of 2FPPD with uncoordinated Pb^{2+}, which enhances the crystallinity of PVK and suppresses the nonradiative recombination of carriers. In addition to the above advantages, the energy level alignment of PSCs is optimized, which reduces the energy barrier and carrier accumulation at the interface. Furthermore, the PCBM&2FPPD interface co-modification strategy also suppresses ion migration and moisture intrusion, which contributes to improving the stability of PSCs. As a result, the PCE increases from 17.01% to 18.36%, in which various photovoltaic parameters (V_{OC}, J_{SC}, FF, and HI) are optimized simultaneously. Moreover, the environmental stability of PSCs is greatly improved due to the protection of PVK by the 2FPPD thin layer, which can be stored stably in air (RH = 10−20%) for about 800 h. This work provides a simple

https://doi.org/10.1021/acsaem.2c02096
ACS Appl. Energy Mater. 2022, 5, 13419−13428

and effective way to prepare efficient and stable PSCs, which illustrates the importance of interface engineering for optimizing the performance and stability of PSCs.

■ ASSOCIATED CONTENT

Supporting Information

The Supporting Information is available free of charge at https://pubs.acs.org/doi/10.1021/acsaem.2c02096.

Experimental Section (including materials, methods, and characterization); schematic of the preparation process of PSCs; $J-V$ curves, water contact angle, precursor solution contact angle, and optical transmission spectra of different ETLs; XPS spectra, VB XPS spectra, UPS spectra, 3D AFM images, AFM phase images, and cross-sectional SEM images of perovskite films; XRD patterns, UV−Vis absorption spectra, steady-state PL spectra, SEM images, grain size distribution, Mott−Schottky plots, Nyquist plots, TPC, TPV, and $J-V$ curves of perovskite films based on different concentrations of PCBM and 2FPPD; dark $J-V$ curves for electron-only devices and hole-only devices; J_{SC} as a function of light intensities curves; statistical distribution of photovoltaic parameters; $J-V$ curves of hysteresis behavior; tables for ETL conductivity, FWHM of the (110) crystal plane diffraction peaks, TRPL parameters, SCLC parameters, and photovoltaic parameters (PDF)

■ AUTHOR INFORMATION

Corresponding Authors

Zhiwen Jin − *School of Physical Science and Technology & Key Laboratory for Magnetism and Magnetic Materials of MoE, Lanzhou University, Lanzhou 730000, China;* orcid.org/0000-0002-5256-9106; Email: lanw@lzu.edu.cn

Wei Lan − *School of Physical Science and Technology & Key Laboratory for Magnetism and Magnetic Materials of MoE, Lanzhou University, Lanzhou 730000, China;* orcid.org/0000-0001-6194-4839; Email: jinzw@lzu.edu.cn

Authors

Hui Guan − *School of Physical Science and Technology & Key Laboratory for Magnetism and Magnetic Materials of MoE, Lanzhou University, Lanzhou 730000, China*

Yutian Lei − *School of Physical Science and Technology & Key Laboratory for Magnetism and Magnetic Materials of MoE, Lanzhou University, Lanzhou 730000, China*

Qiyuan Wu − *School of Physical Science and Technology & Key Laboratory for Magnetism and Magnetic Materials of MoE, Lanzhou University, Lanzhou 730000, China*

Xufeng Zhou − *School of Material Science and Engineering, Liaocheng University, Liaocheng 252000, China*

Haoxu Wang − *Photovoltaic Materials and Devices Group, Delft University of Technology, 2628 CD Delft, The Netherlands;* orcid.org/0000-0002-5430-0899

Gang Wang − *Department of Microelectronic Science and Engineering, School of Physical Science and Technology, Ningbo University, Ningbo 315211, China;* orcid.org/0000-0002-2288-3807

Wenquan Li − *School of Physics and Electronic Information Engineering, Qinghai Normal University, Xining 810008, China*

Complete contact information is available at: https://pubs.acs.org/10.1021/acsaem.2c02096

Notes

The authors declare no competing financial interest.

■ ACKNOWLEDGMENTS

This work was funded by the National Natural Science Foundation of China (22279049, 51902148, 51801088, and 62174093), the Fundamental Research Funds for the Central Universities (lzujbky-2021-59, lzujbky-2021-sp69, and lzujbky-2021-sp50), and the Science and Technology Program of Qinghai Province (2022-ZJ-703).

■ REFERENCES

(1) Zhang, J.; Hodes, G.; Jin, Z.; Liu, S. All-Inorganic $CsPbX_3$ Perovskite Solar Cells: Progress and Prospects. *Angew. Chem., Int. Ed.* **2019**, *58*, 15596−15618.

(2) Li, Z.; Zhou, F.; Wang, Q.; Ding, L.; Jin, Z. Approaches for Thermodynamically Stabilized $CsPbI_3$ Solar Cells. *Nano Energy* **2020**, *71*, No. 104634.

(3) Kojima, A.; Teshima, K.; Shirai, Y.; Miyasaka, T. Organometal Halide Perovskites as Visible-Light Sensitizers for Photovoltaic Cells. *J. Am. Chem. Soc.* **2009**, *131*, 6050−6051.

(4) NREL. *Best Research-Cell Efficiency*. 2022, https://www.nrel.gov/pv/cell-efficiency.html (Accessed2022−06).

(5) Wang, H.; Bian, H.; Jin, Z.; Zhang, H.; Liang, L.; Wen, J.; Wang, Q.; Ding, L.; Liu, S. Cesium Lead Mixed-Halide Perovskites for Low-Energy Loss Solar Cells with Efficiency Beyond 17%. *Chem. Mater.* **2019**, *31*, 6231−6238.

(6) Zhou, Y.; Zhao, Y. Chemical Stability and Instability of Inorganic Halide Perovskites. *Energy Environ. Sci.* **2019**, *12*, 1495−1511.

(7) He, J.; Su, J.; Lin, Z.; Ma, J.; Zhou, L.; Zhang, S.; Liu, S.; Chang, J.; Hao, Y. Enhanced Efficiency and Stability of All-Inorganic $CsPbI_2Br$ Perovskite Solar Cells by Organic and Ionic Mixed Passivation. *Adv. Sci.* **2021**, *8*, 2101367.

(8) Sun, X.; Shao, Z.; Rao, Y.; Meng, H.; Gao, C.; Chen, C.; Liu, D.; Lv, P.; Li, Z.; Wang, X.; Cui, G.; Pang, S. A Low-Temperature Additive-Involved Leaching Method for Highly Efficient Inorganic Perovskite Solar Cells. *Adv. Energy Mater.* **2021**, *11*, 2002754.

(9) Zhang, T.; Wang, F.; Chen, H.; Ji, L.; Wang, Y.; Li, C.; Raschke, M. B.; Li, S. Mediator−Antisolvent Strategy to Stabilize All-Inorganic $CsPbI_3$ for Perovskite Solar Cells with Efficiency Exceeding 16%. *ACS Energy Lett.* **2020**, *5*, 1619−1627.

(10) Ho-Baillie, A.; Zhang, M.; Lau, C. F. J.; Ma, F.-J.; Huang, S. Untapped Potentials of Inorganic Metal Halide Perovskite Solar Cells. *Joule* **2019**, *3*, 938−955.

(11) Chen, H.; Zhou, F.; Jin, Z. Interface Engineering, the Trump-Card for $CsPbX_3$ (X=I, Br) Perovskite Solar Cells Development. *Nano Energy* **2021**, *79*, No. 105490.

(12) Kye, Y.-H.; Yu, C.-J.; Jong, U.-G.; Ri, K.-C.; Kim, J.-S.; Choe, S.-H.; Hong, S.-N.; Li, S.; Wilson, J. N.; Walsh, A. Vacancy-Driven Stabilization of the Cubic Perovskite Polymorph of $CsPbI_3$. *J. Phys. Chem. C* **2019**, *123*, 9735−9744.

(13) Xu, Y.; Wang, M.; Lei, Y.; Ci, Z.; Jin, Z. Crystallization Kinetics in 2D Perovskite Solar Cells. *Adv. Energy Mater.* **2020**, *10*, 2002558.

(14) Liang, J.; Han, X.; Yang, J.-H.; Zhang, B.; Fang, Q.; Zhang, J.; Ai, Q.; Ogle, M. M.; Terlier, T.; Martí, A. A.; Lou, J. Defect-Engineering-Enabled High-Efficiency All-Inorganic Perovskite Solar Cells. *Adv. Mater.* **2019**, *31*, 1903448.

(15) Zhou, F.; Li, Z.; Chen, H.; Wang, Q.; Ding, L.; Jin, Z. Application of Perovskite Nanocrystals (NCs)/Quantum Dots (QDs) in Solar Cells. *Nano Energy* **2020**, *73*, No. 104757.

(16) Luo, D.; Li, X.; Dumont, A.; Yu, H.; Lu, Z.-H. Recent Progress on Perovskite Surfaces and Interfaces in Optoelectronic Devices. *Adv. Mater.* **2021**, *33*, 2006004.

(17) Bai, Y.; Meng, X.; Yang, S. Interface Engineering for Highly Efficient and Stable Planar p-i-n Perovskite Solar Cells. *Adv. Energy Mater.* **2018**, *8*, 1701883.
(18) Bian, H.; Wang, Q.; Yang, S.; Yan, C.; Wang, H.; Liang, L.; Jin, Z.; Wang, G.; Liu, S. Nitrogen-Doped Graphene Quantum Dots for 80% Photoluminescence Quantum Yield for Inorganic γ-$CsPbI_3$ Perovskite Solar Cells with Efficiency Beyond 16%. *J. Mater. Chem. A* **2019**, *7*, 5740−5747.
(19) Yan, C.; Li, Z.; Sun, Y.; Zhao, J.; Huang, X.; Yang, J.; Ci, Z.; Ding, L.; Jin, Z. Decreasing Energy Loss and Optimizing Band Alignment for High Performance $CsPbI_3$ Solar Cells Through Guanidine Hydrobromide Post-Treatment. *J. Mater. Chem. A* **2020**, *8*, 10346−10353.
(20) Wang, X.; Wang, Y.; Chen, Y.; Liu, X.; Zhao, Y. Efficient and Stable $CsPbI_3$ Inorganic Perovskite Photovoltaics Enabled by Crystal Secondary Growth. *Adv. Mater.* **2021**, *33*, 2103688.
(21) Xiang, W.; Liu, S.; Tress, W. Interfaces and Interfacial Layers in Inorganic Perovskite Solar Cells. *Angew. Chem., Int. Ed.* **2021**, *60*, 26440−26453.
(22) Li, B.; Li, Z.; Wu, X.; Zhu, Z. Interface Functionalization in Inverted Perovskite Solar Cells: From Material Perspective. *Nano Res. Energy* **2022**, *1*, No. e9120011.
(23) Xu, H.; Miao, Y.; Wei, N.; Chen, H.; Qin, Z.; Liu, X.; Wang, X.; Qi, Y.; Zhang, T.; Zhao, Y. CsI Enhanced Buried Interface for Efficient and UV-Robust Perovskite Solar Cells. *Adv. Energy Mater.* **2021**, *12*, 2103151.
(24) Levine, I.; Al-Ashouri, A.; Musiienko, A.; Hempel, H.; Magomedov, A.; Drevilkauskaite, A.; Getautis, V.; Menzel, D.; Hinrichs, K.; Unold, T.; Albrecht, S.; Dittrich, T. Charge Transfer Rates and Electron Trapping at Buried Interfaces of Perovskite Solar Cells. *Joule* **2021**, *5*, 2915−2933.
(25) Xiong, Z.; Chen, X.; Zhang, B.; Odunmbaku, G. O.; Ou, Z.; Guo, B.; Yang, K.; Kan, Z.; Lu, S.; Chen, S.; Ouedraogo, N. A. N.; Cho, Y.; Yang, C.; Chen, J.; Sun, K. Simultaneous Interfacial Modification and Crystallization Control by Biguanide Hydrochloride for Stable Perovskite Solar Cell with PCE of 24.4%. *Adv. Mater.* **2021**, *34*, 2106118.
(26) Zeng, J.; Bi, L.; Cheng, Y.; Xu, B.; Jen, A. K.-Y. Self-Assembled Monolayer Enabling Improved Buried Interfaces in Blade-Coated Perovskite Solar Cells for High Efficiency and Stability. *Nano Research Energy* **2022**, *1*, No. e9120004.
(27) Leijtens, T.; Eperon, G. E.; Pathak, S.; Abate, A.; Lee, M. M.; Snaith, H. J. Overcoming Ultraviolet Light Instability of Sensitized TiO_2 With Meso-Superstructured Organometal Tri-Halide Perovskite Solar Cells. *Nat. Commun.* **2013**, *4*, 2885.
(28) Gong, X.; Sun, Q.; Liu, S.; Liao, P.; Shen, Y.; Gätzel, C.; Zakeeruddin, S. M.; Gätzel, M.; Wang, M. Highly Efficient Perovskite Solar Cells with Gradient Bilayer Electron Transport Materials. *Nano Lett.* **2018**, *18*, 3969−3977.
(29) Hu, W.; Wen, Z.; Yu, X.; Qian, P.; Lian, W.; Li, X.; Shang, Y.; Wu, X.; Chen, T.; Lu, Y.; Wang, M.; Yang, S. In Situ Surface Fluorination of TiO_2 Nanocrystals Reinforces Interface Binding of Perovskite Layer for Highly Efficient Solar Cells with Dramatically Enhanced Ultraviolet-Light Stability. *Adv. Sci.* **2021**, *8*, 2004662.
(30) Wang, B.; Yang, J.; Lu, L.; Xiao, W.; Wu, H.; Xiong, S.; Tang, J.; Duan, C.; Bao, Q. Interface Engineering of Air-Stable n-Doping Fullerene-Modified TiO_2 Electron Transport Layer for Highly Efficient and Stable Perovskite Solar Cells. *Adv. Mater. Interfaces* **2020**, *7*, 1901964.
(31) Liu, G.; Zheng, H.; Xu, H.; Zhang, L.; Xu, X.; Xu, S.; Pan, X. Interface Passivation Treatment by Halogenated Low-Dimensional Perovskites for High-Performance and Stable Perovskite Photovoltaics. *Nano Energy* **2020**, *73*, No. 104753.
(32) Zhang, Z.; Gao, Y.; Li, Z.; Qiao, L.; Xiong, Q.; Deng, L.; Zhang, Z.; Long, R.; Zhou, Q.; Du, Y.; Lan, Z.; Zhao, Y.; Li, C.; Müllen, K.; Gao, P. Marked Passivation Effect of Naphthalene-1,8-Dicarboximides in High-Performance Perovskite Solar Cells. *Adv. Mater.* **2021**, *33*, 2008405.
(33) Liu, G.; Zheng, H.; Ye, J.; Xu, S.; Zhang, L.; Xu, H.; Liang, Z.; Chen, X.; Pan, X. Mixed-Phase Low-Dimensional Perovskite-Assisted Interfacial Lead Directional Management for Stable Perovskite Solar Cells with Efficiency over 24%. *ACS Energy Lett.* **2021**, *6*, 4395−4404.
(34) Su, P.; Bai, L.; Bi, H.; Liu, B.; He, D.; Wang, W.; Cao, X.; Chen, S.; Lee, D.; Yang, H.; Zang, Z.; Chen, J. Crystal Orientation Modulation and Defect Passivation for Efficient and Stable Methylammonium-Free Dion-Jacobson Quasi-2D Perovskite Solar Cells. *ACS Appl. Mater. Interfaces* **2021**, *13*, 29567−29575.
(35) Wang, H.; Dong, Z.; Liu, H.; Li, W.; Zhu, L.; Chen, H. Roles of Organic Molecules in Inorganic $CsPbX_3$ Perovskite Solar Cells. *Adv. Energy Mater.* **2021**, *11*, 2002940.
(36) Long, C.; Huang, K.; Chang, J.; Zuo, C.; Gao, Y.; Luo, X.; Liu, B.; Xie, H.; Chen, Z.; He, J.; Huang, H.; Gao, Y.; Ding, L.; Yang, J. Creating a Dual-Functional 2D Perovskite Layer at the Interface to Enhance the Performance of Flexible Perovskite Solar Cells. *Small* **2021**, *17*, 2102368.
(37) Zhang, J.; Wang, L.; Jiang, C.; Cheng, B.; Chen, T.; Yu, J. $CsPbBr_3$ Nanocrystal Induced Bilateral Interface Modification for Efficient Planar Perovskite Solar Cells. *Adv. Sci.* **2021**, *8*, 2102648.
(38) Gharibzadeh, S.; Fassl, P.; Hossain, I. M.; Rohrbeck, P.; Frericks, M.; Schmidt, M.; Duong, T.; Khan, M. R.; Abzieher, T.; Nejand, B. A.; Schackmar, F.; Almora, O.; Feeney, T.; Singh, R.; Fuchs, D.; Lemmer, U.; Hofmann, J. P.; Weber, S. A. L.; Paetzold, U. W. Two Birds with One Stone: Dual Grain-Boundary and Interface Passivation Enables >22% Efficient Inverted Methylammonium-Free Perovskite Solar Cells. *Energy Environ. Sci.* **2021**, *14*, 5875−5893.
(39) Chen, Y.; Zuo, X.; He, Y.; Qian, F.; Zuo, S.; Zhang, Y.; Liang, L.; Chen, Z.; Zhao, K.; Liu, Z.; Gou, J.; Liu, S. Dual Passivation of Perovskite and SnO_2 for High-Efficiency $MAPbI_3$ Perovskite Solar Cells. *Adv. Sci.* **2021**, *8*, 2001466.
(40) Wang, M.; Yin, Y.; Cai, W.; Liu, J.; Han, Y.; Feng, Y.; Dong, Q.; Wang, Y.; Bian, J.; Shi, Y. Synergetic Co-Modulation of Crystallization and Co-Passivation of Defects for $FAPbI_3$ Perovskite Solar Cells. *Adv. Funct. Mater.* **2021**, *32*, 2108567.
(41) Ma, J.; Su, J.; Lin, Z.; He, J.; Zhou, L.; Li, T.; Zhang, J.; Liu, S.; Chang, J.; Hao, Y. Double Side Interfacial Optimization for Low-Temperature Stable $CsPbI_2Br$ Perovskite Solar Cells with High Efficiency Beyond 16%. *Energy Environ. Mater.* **2022**, *5*, 637−644.
(42) Zhang, Y.; Wang, Y.; Zhao, L.; Yang, X.; Hou, C.-H.; Wu, J.; Su, R.; Jia, S.; Shyue, J.-J.; Luo, D.; Chen, P.; Yu, M.; Li, Q.; Li, L.; Gong, Q.; Zhu, R. Depth-Dependent Defect Manipulation in Perovskites for High-Performance Solar Cells. *Energy Environ. Sci.* **2021**, *14*, 6526−6535.
(43) Choi, K.; Lee, J.; Kim, H. I.; Park, C. W.; Kim, G.-W.; Choi, H.; Park, S.; Park, S. A.; Park, T. Thermally Stable, Planar Hybrid Perovskite Solar Cells with High Efficiency. *Energy Environ. Sci.* **2018**, *11*, 3238−3247.
(44) Zhuang, J.; Mao, P.; Luan, Y.; Chen, N.; Cao, X.; Niu, G.; Jia, F.; Wang, F.; Cao, S.; Wang, J. Rubidium Fluoride Modified SnO_2 for Planar n-i-p Perovskite Solar Cells. *Adv. Funct. Mater.* **2021**, *31*, 2010385.
(45) Wang, Y.; Liu, X.; Zhang, T.; Wang, X.; Kan, M.; Shi, J.; Zhao, Y. The Role of Dimethylammonium Iodide in $CsPbI_3$ Perovskite Fabrication: Additive or Dopant? *Angew. Chem., Int. Ed.* **2019**, *58*, 16691−16696.
(46) Gu, X.; Xiang, W.; Tian, Q.; Liu, S. Rational Surface-Defect Control via Designed Passivation for High-Efficiency Inorganic Perovskite Solar Cells. *Angew. Chem., Int. Ed.* **2021**, *60*, 23164−23170.
(47) Zhang, J.; Bai, D.; Jin, Z.; Bian, H.; Wang, K.; Sun, J.; Wang, Q.; Liu, S. 3D−2D−0D Interface Profiling for Record Efficiency All-Inorganic $CsPbBrI_2$ Perovskite Solar Cells with Superior Stability. *Adv. Energy Mater.* **2018**, *8*, 1703246.
(48) Zhu, H.; Ren, Y.; Pan, L.; Ouellette, O.; Eickemeyer, F. T.; Wu, Y.; Li, X.; Wang, S.; Liu, H.; Dong, X.; Zakeeruddin, S. M.; Liu, Y.; Hagfeldt, A.; Gätzel, M. Synergistic Effect of Fluorinated Passivator and Hole Transport Dopant Enables Stable Perovskite Solar Cells with an Efficiency Near 24%. *J. Am. Chem. Soc.* **2021**, *143*, 3231−3237.

https://doi.org/10.1021/acsaem.2c02096
ACS Appl. Energy Mater. 2022, 5, 13419−13428

(49) Wang, Q.; Lin, Z.; Su, J.; Xu, Y.; Guo, X.; Li, Y.; Zhang, M.; Zhang, J.; Chang, J.; Hao, Y. Dithiol Surface Treatment Towards Improved Charge Transfer Dynamic and Reduced Lead Leakage in Lead Halide Perovskite Solar Cells. *EcoMat* **2022**, *4*, No. e12185.
(50) Zhao, R.; Xie, L.; Zhuang, R.; Wu, T.; Zhao, R.; Wang, L.; Sun, L.; Hua, Y. Interfacial Defect Passivation and Charge Carrier Management for Efficient Perovskite Solar Cells via a Highly Crystalline Small Molecule. *ACS Energy Lett.* **2021**, *6*, 4209−4219.
(51) Wang, L.; Wang, X.; Zhu, L.; Leng, S.-B.; Liang, J.; Zheng, Y.; Zhang, Z.; Zhang, Z.; Liu, X.; Liu, F.; Chen, C.-C. Favorable Grain Growth of Thermally Stable Formamidinium-Methylammonium Perovskite Solar Cells by Hydrazine Chloride. *Chem. Eng. J.* **2022**, *430*, No. 132730.
(52) Yang, D.; Yang, R.; Wang, K.; Wu, C.; Zhu, X.; Feng, J.; Ren, X.; Fang, G.; Priya, S.; Liu, S. High Efficiency Planar-Type Perovskite Solar Cells with Negligible Hysteresis Using EDTA-Complexed SnO_2. *Nat. Commun.* **2018**, *9*, 3239.
(53) Li, W.; Gu, X.; Shan, C.; Lai, X.; Sun, X. W.; Kyaw, A. K. K. Efficient and Stable Mesoscopic Perovskite Solar Cell in High Humidity by Localized Dion-Jacobson 2D-3D Heterostructures. *Nano Energy* **2022**, *91*, No. 106666.
(54) Sun, H.; Deng, K.; Jiang, Y.; Ni, J.; Xiong, J.; Li, L. Realizing Stable Artificial Photon Energy Harvesting Based on Perovskite Solar Cells for Diverse Applications. *Small* **2020**, *16*, 1906681.
(55) Han, Y.; Zhao, H.; Duan, C.; Yang, S.; Yang, Z.; Liu, Z.; Liu, S. Controlled n-Doping in Air-Stable $CsPbI_2Br$ Perovskite Solar Cells with a Record Efficiency of 16.79%. *Adv. Funct. Mater.* **2020**, *30*, 1909972.
(56) Dou, J.; Zhu, C.; Wang, H.; Han, Y.; Ma, S.; Niu, X.; Li, N.; Shi, C.; Qiu, Z.; Zhou, H.; Bai, Y.; Chen, Q. Synergistic Effects of Eu-MOF on Perovskite Solar Cells with Improved Stability. *Adv. Mater.* **2021**, *33*, 2102947.
(57) Ma, S.; Bai, Y.; Wang, H.; Zai, H.; Wu, J.; Li, L.; Xiang, S.; Liu, N.; Liu, L.; Zhu, C.; Liu, G.; Niu, X.; Chen, H.; Zhou, H.; Li, Y.; Chen, Q. 1000 h Operational Lifetime Perovskite Solar Cells by Ambient Melting Encapsulation. *Adv. Energy Mater.* **2020**, *10*, 1902472.
(58) Duan, J.; Zhao, Y.; He, B.; Tang, Q. High-Purity Inorganic Perovskite Films for Solar Cells with 9.72% Efficiency. *Angew. Chem., Int. Ed.* **2018**, *57*, 3787−3791.
(59) Wang, M.; Lei, Y.; Xu, Y.; Han, L.; Ci, Z.; Jin, Z. The J−V Hysteresis Behavior and Solutions in Perovskite Solar Cells. *Sol. RRL* **2020**, *4*, 2000586.
(60) Xiong, Q.; Wang, C.; Zhou, Q.; Wang, L.; Wang, X.; Yang, L.; Ding, J.; Chen, C.-c.; Wu, J.; Li, X.; Gao, P. Rear Interface Engineering to Suppress Migration of Iodide Ions for Efficient Perovskite Solar Cells with Minimized Hysteresis. *Adv. Funct. Mater.* **2021**, *32*, 2107823.
(61) Chen, Y.; Zhou, W.; Chen, X.; Zhang, X.; Gao, H.; Ouedraogo, N. A. N.; Zheng, Z.; Han, C. B.; Zhang, Y.; Yan, H. In Situ Management of Ions Migration to Control Hysteresis Effect for Planar Heterojunction Perovskite Solar Cells. *Adv. Funct. Mater.* **2021**, *32*, 2108417.

https://doi.org/10.1021/acsaem.2c02096
ACS Appl. Energy Mater. 2022, 5, 13419−13428